Research Article

Study on the Effect of Oxidative Jet and Vortex Structure in Fluidic Throat Combined with Thrust Vector Control

Dongfeng Yan [ID], Yi Xiao, Lu Ye, Ganchao Zhao, and Liang Wang

Flight Technology College, Civil Aviation Flight University of China, Guanghan 618307, China

Correspondence should be addressed to Dongfeng Yan; yandongfeng@cafuc.edu.cn

To examine the impact of oxidative jets on the thrust vector angle, secondary combustion efficiency, and combustion chamber pressure, inert gas (nitrogen) and pure oxygen are injected into the primary flow, which includes combustible components, at various locations in the divergence section and throat using different injection techniques. The simulations utilize Reynolds-averaged Navier-Stokes equations coupled with the SST k-ω turbulence model in two-dimensional numerical simulations and large-eddy simulation in three-dimensional studies. The numerical method is validated through schlieren experiments, and the vortex is identified using the Liutex-Omega method. The vortex structures and flow characteristics are analyzed. The results indicate that, at the same flow rate, the vector control effect of pure oxygen is superior to nitrogen only in the divergence section, but inferior to nitrogen in both the divergence section and throat. However, with improved vector control, the peak of the vector angle is achieved at a lower flow rate in the case of pure oxygen. When the secondary flow is introduced only in the divergence section, the flow ratio corresponding to the peak point in the pure oxygen case is approximately 14.3% earlier than that in the nitrogen case. The introduction of the pure oxygen jet enhances the secondary combustion efficiency of the primary flow, but to a limited extent. Additionally, when the jet is introduced at the throat, the effect of the pure oxygen case on adjusting the combustion chamber pressure is inferior to that of the nitrogen case. Concerning flow details, the trailing lower vortex replaces the trailing major vortex to become the highest magnitude vortex when the momentum flux ratio is small.

1. Introduction

The control of thrust, both in magnitude and direction, is crucial in solid rocket motor engineering. This control plays a significant role in increasing the flight range of aircraft, improving maneuverability, and reducing the impact of the environment on the aircraft [1–4]. However, adjusting thrust for solid rocket motors is challenging because the solid propellant burns continuously and uncontrollably once ignited, until all the propellant is consumed [5, 6]. After years of research and development, the technology for adjusting solid rocket motor thrust has made significant progress [7, 8]. The aerodynamic variable nozzle/fluidic nozzle throat (FNT) is a technology that changes the flow area of the primary flow through the interaction between the secondary flow (jet) and primary flows. This technology exhibits high reliability and has no drive mechanism. The concept has been successfully applied to liquid rocket

motors, aeroengines, and solid rocket motors [1, 9, 10]. The thrust magnitude and direction can be simultaneously controlled by injecting secondary flow into the nozzle throat and divergence section [9].

The fluidic throat scheme, also known as the aerodynamic throat, involves injecting secondary flow into the nozzle throat to squeeze the primary flow, thereby changing the pressure of the combustion chamber and adjusting thrust. This scheme was first applied to solid rocket engines by Ali et al. in 2012, who conducted a series of research on it [11]. From 2009 to 2020, Xie et al. conducted long-term, in-depth research on the fluidic throat scheme and made significant progress in various areas, including steady-state performance, dynamic performance, atomization, damping, and thermal tests. These findings verified the feasibility of the fluidic throat scheme in solid rocket engines [1, 4, 9, 12].

The shock vector control (SVC) or thrust vector control (TVC) method involves injecting secondary flow into the

divergence section of the nozzle to generate induced shock waves that deflect the primary flow and alter the direction of thrust [13–15]. This technique has been implemented in missiles such as the Minuteman 3 ICBM and the Julang 2 ICBM and has undergone significant advancements in recent years [13, 16–19]. Semlitsch and Mihăescu investigated fluidic injection scenarios for shock patternability and identified the optimal configuration of shock control and thrust [16, 19]. Neely et al. and Wang et al. conducted experimental studies on shock-induced vectors, including regulation performance and instability analysis [20, 21]. Zhang et al. examined the application of shock vector control in a pulse detonation tube [22]. Furthermore, 3D detailed simulations and sensitivity analyses have rapidly progressed in this area [23–25].

Adjusting the magnitude and direction of thrust is possible by incorporating injection ports in the nozzle throat and divergence section. Significant advancements have been made in regulating thrust magnitude and direction separately, and there has been some research on the combined injection method through simulation and cold flow experiments. However, studies on the secondary combustion of the oxidative jet with the primary flow in a combined injection scheme are scarce. The chemical reaction produced by secondary combustion plays a crucial role in determining both the magnitude and direction of thrust. Currently, most propellants are in a state of negative oxygen equilibrium, which means that their combustion products contain unoxidized components. When these products come into contact with air, they undergo secondary combustion, releasing additional heat. By injecting an oxidizing gas (such as pure oxygen or air) into the throat of the nozzle, the primary flow undergoes preburning, resulting in increased heat release and improved thermal resistance of the nozzle's throat. This, in turn, enhances the nozzle's choke performance and thrust regulation ratio [9, 26, 27].

The flow field within a rocket motor is a region of transonic flow with limited space and a complex wave system. When a jet is sprayed into a high-speed crossflow, both flows are altered, resulting in a sharp exchange of momentum and energy between them [28, 29]. The primary flow causes the jet to bend and deflect, producing intricate vortex structures. Presently, research on shock vector control (SVC) and fluidic nozzle throat (FNT) technology primarily focuses on engineering applications, but there is a lack of research on the underlying flow mechanism [10].

This paper explores the combination of FNT and SVC by developing a plane model and an axisymmetric model that allow for oxidative jet injection at 90° into the nozzle throat and divergence section. A two-dimensional numerical simulation method is utilized to investigate the effects of the oxidative jet on the thrust vector angle, secondary combustion efficiency, and combustion chamber pressure. Additionally, three-dimensional large-eddy simulations are conducted to examine the flow characteristics and details, and the vortex structure is identified using the Liutex-Omega method. This approach is aimed at providing a deeper understanding of the flow mechanism and at optimizing the thrust control in rocket motor engineering.

2. Calculation Model and Numerical Method

2.1. Calculation Model and Boundary Conditions. The physical model used for the two-dimensional study is a planar nozzle. The throat diameter is 9.6 mm, the injection port diameter is 0.96 mm, and the nozzle convergence half-angle and expansion half-angle are 45° and 15°, respectively. The expansion ratio is approximately 3.757. The motor is designed for a thrust of 400 N without the injection of secondary flow, and the working pressure of the combustion chamber is 2 MPa. The inlets of the primary and secondary flows are set as mass flow inlets. The primary flow has a flow rate of 11.78 kg/s and an injection angle of 90°. The outlet is a pressure outlet with a pressure of 101 kPa and a temperature of 300 K. No-slip conditions are used at the walls, along with an adiabatic wall and zero normal pressure gradient. The geometric model used in this simulation is based on reference [12]. The grid shown in Figure 1 is refined near the throat and injection port. The computational domain measures $152 \times 45 \text{ mm}^2$, which is covered by 11.5×10^4 grid cells. To accurately describe the position of the injection port, the relative positions of the injection port, throat, nozzle, and divergence section are defined quantitatively in this paper, as shown in Figure 2. In this paper, D_t represents the diameter of the nozzle throat, and D_i represents the distance between the injection port in the divergence section and the nozzle throat. The ratio of D_i/D_t is 0.9 in this study.

Figure 3 shows the 3D model used in the study, with a throat diameter of 9.6 mm and an injection port diameter of 1.76 mm. The calculation domain measures $80 \times 90 \times 45 \text{ mm}^3$, covered by 2.98×10^6 grid cells. The 3D model is primarily utilized to study flow details, and the fluid working medium used is ideal air. On the other hand, the 2D model focuses on examining the thrust vector's adjustment characteristics of the oxidative jet, with the working medium being gas.

Refer to a certain type of double-base propellant for its components and proportions at the exit of the combustion chamber, as shown in Table 1 (the influence of solid particle Al_2O_3 is ignored in the calculation).

This study injects the oxidative jet at the nozzle throat and divergence section, resulting in a two-step chemical reaction with the primary flow components. The chemical mechanism utilized for the secondary combustion of the primary flow employs a one-step total inclusion irreversible reaction. The specific reaction is as follows:

$$\begin{aligned} CO + 0.5\,O_2 &\longrightarrow CO_2 \\ H_2 + 0.5\,O_2 &\longrightarrow H_2O \end{aligned} \tag{1}$$
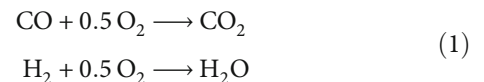
The setting of chemical reaction is directly based on the reaction of carbon monoxide-air and hydrogen-air in Fluent database [30], and the kinetic parameters are shown in Table 2.

The mechanism for secondary gas combustion can either be a flamelet in an eddy regime or a reaction sheet regime. A higher Mach number increases the likelihood of a flame mechanism in the vortex. Thus, in supersonic conditions,
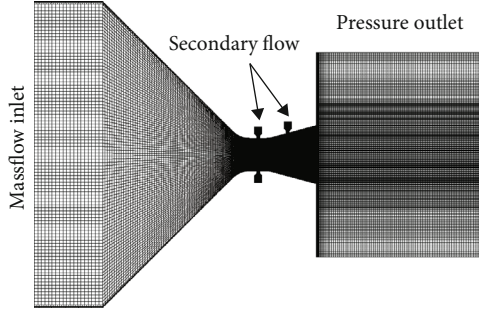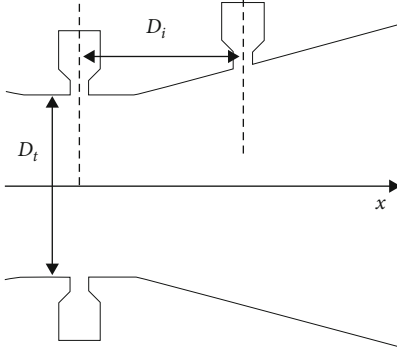
Figure 1: Mesh and boundary condition.

Figure 2: Schematic diagram of injection port position.

turbulent-chemical kinetic coupling can be described using the vortex dissipation concept, where turbulent mixing and chemical reaction kinetics govern the reaction rate. The net rate of composition generation is determined by the lower value of the following two expressions [31]:

$$
R_{i,r} = v'_{i,r} M_{w,i} AB\rho \frac{\varepsilon}{k} \frac{\sum_P Y_P}{\sum_j^N v''_{j,r} M_{w,j}},
$$

$$
R_{i,r} = v'_{i,r} M_{w,i} A\rho \frac{\varepsilon}{k} \min_{\Re} \left(\frac{Y_{\Re}}{v'_{\Re,r} M_{w,\Re}} \right),
$$

(2)

where Y_P is mass fraction of combustion product P, $Y_{\Re}$ is the mass fraction of a particular reactant $\Re$. Based on experience, $A = 4.0$ and $B = 0.5$.

Given that the temperature of the primary flow is 3000 K, it is expected that pure oxygen will undergo secondary combustion with the primary flow once it is injected. On the other hand, when the inert jet is injected, it is assumed that no secondary combustion or chemical reaction occurs in the entire flow field. The temperature of the secondary flow, including the oxidative jet and inert jet, is 300 K. This paper establishes four research examples based on different combinations of injection working fluids and positions, namely, Case 1: nitrogen injection in the divergence section, Case 2: pure oxygen injection in the divergence section, Case 3: nitrogen injection in the divergence section and throat, and Case 4: pure oxygen injection in the divergence section and throat, as shown in Table 3.

2.2. Numerical Methods. During the injection process, various parts of the motor combustion chamber and nozzle are subject to complex physical and chemical processes. In order to simplify the calculation, the following assumptions are introduced:

(1) The flow is assumed to be single phase, disregarding any solid particles in the propellant that may not be completely burned

(2) The mixed gas is assumed to be an ideal gas that satisfies the ideal gas equation

(3) Radiation and gravity effects are not considered

(4) The walls are assumed to be adiabatic, and there is no heat exchange between the entire flow field and the external system

Two numerical methods were employed for the calculations: RANS coupled with the SST k-ω turbulence model and large-eddy simulation (LES). The SST k-ω turbulence model is commonly used in computational fluid dynamics for pressure gradient flow calculations. It is suitable for near-wall and far-wall applications due to its consideration of crossdiffusion terms [18, 32, 33]. The SST k-ω model was used for the 2D and 3D initial flow field calculations, while LES was utilized to study the detailed 3D flow characteristics.

The compressible RANS equation for air can be written in Cartesian tensor form as

$$
\frac{\partial \rho}{\partial t} + \frac{\partial}{\partial x_i} (\rho u_i) = 0,
$$

$$
\frac{\partial}{\partial t} (\rho u_i) + \frac{\partial}{\partial x_j} (\rho u_i u_j) = -\frac{\partial p}{\partial x_i} + \frac{\partial}{\partial x_j} \left[\mu \left(\frac{\partial u_i}{\partial x_j} + \frac{\partial u_j}{\partial x_i} - \frac{2}{3} \delta_{ij} \frac{\partial u_l}{\partial x_l} \right) \right]
$$
$$
+ \frac{\partial}{\partial x_j} \left(-\rho \overline{u'_i u'_j} \right),
$$

(3)

where u_i represents the Reynolds mean velocity component with the mean sign omitted, ρ is the density, p is the pressure, u'_i is the fluctuating velocity, μ is the dynamic viscosity, and δ_{ij} is Kronecker's delta.

The conservation equation of this model is as follows:

$$
\frac{\partial}{\partial t} (\rho k) + \frac{\partial}{\partial x_i} (\rho k u i) = \frac{\partial}{\partial x_j} \left(\Gamma_k \frac{\partial k}{\partial x_j} \right) + G_k - Y_k + S_k,
$$

$$
\frac{\partial (\rho \omega)}{\partial t} + \frac{\partial (\rho \omega u_i)}{\partial x_i} = \frac{\partial}{\partial x_j} \left(\Gamma_\omega \frac{\partial \omega}{\partial x_j} \right) + G_\omega - Y_\omega + D_\omega + S_\omega.
$$

(4)

In the equation, k represents turbulent kinetic energy, ω represents specific dissipation rate, G_k represents the production term of turbulent kinetic energy due to the average velocity gradient, and G_ω represents the production term
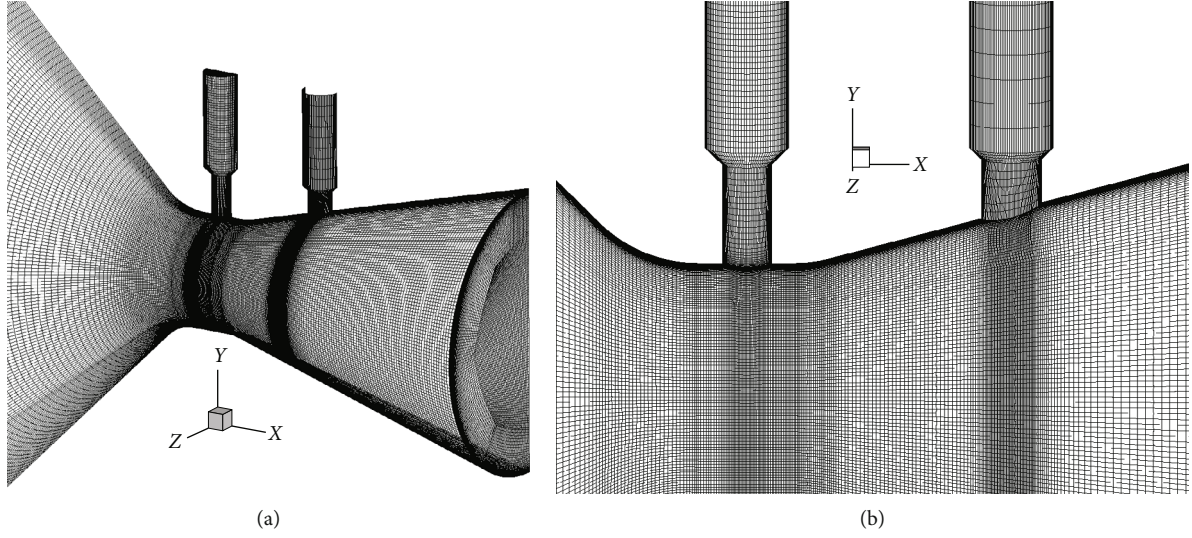
(a)

(b)

FIGURE 3: The three-dimensional grid: (a) global grid; (b) key area of grid.

TABLE 1: Components of primary flow.

Gas components	CO	CO_2	H_2	H_2O	N_2	Al_2O_3
Mass fraction	28%	38%	4%	19%	14.6%	—

TABLE 2: Chemical reaction mechanism.

Reaction	Preexponential factor	Activation energy (J/kgmol)	Temperature exponent
$CO + 0.5\,O_2 \longrightarrow CO_2$	2.239×10^{12}	1.7×10^8	0
$H_2 + 0.5\,O_2 \longrightarrow H_2O$	9.87×10^8	3.1×10^7	0

TABLE 3: Injection schemes of jet.

Injection position	Throat	Divergence section
Case 1	—	Inert gas-N_2
Case 2	—	Pure oxygen-O_2
Case 3	Inert gas-N_2	Inert gas-N_2
Case 4	Pure oxygen-O_2	Pure oxygen-O_2

of specific dissipation rate ω. Γ_k and Γ_ω represent the effective diffusion coefficients of k and ω, respectively. Y_k and Y_ω represent the dissipation of k and ω caused by turbulence. S_k and S_ω are custom source terms, and D_ω represents the crossdiffusion terms.

The SST k-ω model is based on the standard k-ω model and the standard k-ε. In order to connect the two models, the equations of the standard k-ω model are exchanged on the basis of k and ω, and crossdiffusion term D_ω is introduced. The specific definition and parameters can refer to *Fluent Theory Guide* published by Ansys Inc and literatures [34–36].

The governing equations employed for LES are obtained by filtering the time-dependent Navier-Stokes equations in Fourier space or the configuration space. The filtering process effectively filters out the eddies with scales smaller than the filter width or grid spacing used in the computations. Therefore, the resulting equations govern the dynamics of large eddies.

A filtered variable is defined by

$$\overline{\phi}(x) = \int_D \phi\left(x'\right) G\left(x, x'\right) dx', \tag{5}$$

where D is the fluid domain and G is the filter function that determines the scale of the resolved eddies.

Filtering the continuity and momentum equations, we obtain

$$\frac{\partial \rho}{\partial t} + \frac{\partial}{\partial x_i}\left(\rho \overline{u}_i\right) = 0,$$

$$\frac{\partial}{\partial t}\left(\rho \overline{u}_i\right) + \frac{\partial}{\partial x_j}\left(\rho \overline{u}_i \overline{u}_j\right) = \frac{\partial}{\partial x_j}\left(\sigma_{ij}\right) - \frac{\partial \overline{p}}{\partial x_i} - \frac{\partial \tau_{ij}}{\partial x_j}, \tag{6}$$

where σ_{ij} is the stress tensor due to molecular viscosity,

defined by

$$\sigma_{ij} = \left[\mu \left(\frac{\partial \bar{u}_i}{\partial x_j} + \frac{\partial \bar{u}_j}{\partial x_i} \right) \right] - \frac{2}{3} \mu \frac{\partial \bar{u}_l}{\partial x_l} \delta_{ij}, \quad (7)$$

and τ_{ij} is the subgrid-scale (SGS) stress, defined by

$$\tau_{ij} = \rho \overline{u_i u_j} - \rho \bar{u}_i \bar{u}_j. \quad (8)$$

The subgrid-scale stress term represents the momentum exchange between the large- and small-scale pulsations obtained after filtering.

Wall-adapting local eddy viscosity (WALE) is used in this study. The WALE model proposed by Nicoud and Ducros [37] is designed to reproduce more accurate scaling for simulations that contain wall boundary conditions. It includes the effects of both the strain and the rotation and thus provides better predictions in regions where vorticity dominates the irrotational strain. The WALE model reproduces proper near-wall scaling such that the eddy viscosity is $\mu_t = O(y^3)$. The specific definition and parameters can refer to *ANSYS Fluent Theory Guide* published by Ansys Inc [36].

The energy equation can also be found in *ANSYS Fluent Theory Guide*, which is only briefly described here.

$$\frac{\partial}{\partial t}(\rho E) + \nabla \left(\vec{v}(\rho E + p) \right) = \nabla \left(k_{\text{eff}} \nabla T - \sum_j h_j \vec{J}_j + \left(\bar{\bar{\tau}}_{\text{eff}} \cdot \vec{v} \right) \right) + S_h, \quad (9)$$

where k_{eff} is the effective conductivity ($k + k_t$, where k_t is the turbulent thermal conductivity, defined according to the turbulence model being used), and $\vec{J}_j$ is the diffusion flux of species j. The first three terms on the right-hand side represent energy transfer due to conduction, species diffusion, and viscous dissipation, respectively. S_h includes volumetric heat sources that you have defined but not the heat sources generated by finite-rate volumetric or surface reactions since species formation enthalpy is already included in the total enthalpy calculation.

The numerical method is based on the finite volume method [38]. The pressure-based Navier-Stokes solution algorithm in Fluent® is used to solve the governing equations. The gradient interpolation is based on the least-squares cell method, and second-order pressure interpolation is performed. The momentum equation uses a bounded central differencing scheme. The density and energy equations are applied in the second-order upwind format. The SIMPLEC algorithm is used for the pressure–velocity coupling. The time transient term is discretized in a second-order implicit scheme. The time step size of LES is 1×10^{-8} s.

2.3. Vortex Identification Method. In 2016, Liu et al. [39] developed the Ω vortex identification method, which proposed for the first time the further decomposition of vorticity into rotating and nonrotating parts. It also overcame the problem of manual threshold adjustment required by the

second generation of vortex recognition methods. In 2018, Dong et al. [40] proposed the determination of ε for the Ω method, where ε is a small positive parameter used to avoid division by zero. The rotational part of the vorticity is defined as the Liutex or Rortex vector, which can clearly represent both the direction and magnitude of rotational motion. Originally named Rortex, it was renamed Liutex in December 2018, and its derivation process and definition have been described by Liu et al. [39] and Gao and Liu [41]. In 2019, Omega-Liutex Ω_R, which combines the Omega and Liutex/Rortex methods, was proposed [42]. The Ω_R method is able to measure the relative rotation strength and separate the rotational vortices from the shear layers.

Liu et al. have pointed out that vortices cannot be accurately represented solely by vorticity and that it is necessary to decompose vorticity into rotational and nonrotational components [39]. Building on the concept of Liutex, the relationship between vorticity and Liutex was defined as $\nabla \times \mathbf{V} = \mathbf{R} + \mathbf{S}$, where the vorticity is comprised of Liutex and the antisymmetric shear.

The Liutex magnitude is defined as the absolute strength of the vortex, which represents the angular speed of the rigid rotation part of the fluid motion [43].

3. Calculation Verification

3.1. Two-Dimensional Calculation Verification. To validate the numerical calculation method employed in this paper, the Grid Convergence Index (GCI) proposed by Roache [44, 45] is employed for verification. To verify the numerical calculation method used in this paper, the "mass flow ratio = 0.2" case was chosen for verification using the Grid Convergence Index (GCI) proposed by Roache [41, 42]. The three grid scales used were 75,000 for the coarse grid, 89,000 for the medium grid, and 115,000 for the fine grid. The axial wall pressure distribution is presented in Figure 4(a)). The maximum value of GCI23, which represents the convergence index between the medium and fine mesh, is 0.085 as shown in Figure 4(b)). This value is within the range acceptable for engineering calculations. It is worth noting that all two-dimensional calculations in this paper are based on the fine grid.

Furthermore, the experimental model proposed by Waithe and Deere [46] is chosen to validate the numerical calculation method employed in this paper. Waithe and Deere conducted numerous experiments at the Langley Research Center to investigate the vector performance of nozzles with different numbers of injection ports under varying nozzle pressure ratios and injection pressure ratios.

In this paper, one of the operational conditions is used to verify the numerical algorithm. Based on the experimental conditions, the calculated inlet conditions are as follows: the total inlet pressure is 466,095 Pa, and the total temperature is 308.15 K, corresponding to a nozzle pressure ratio of 3.7. The solid wall surface is modeled as a nonslip adiabatic wall. The total inlet pressure of the secondary flow is 326,266.5 Pa, and the total temperature is 308.15 K, corresponding to a nozzle pressure ratio of 0.7. The flow at the nozzle outlet is supersonic, and the flow parameters are
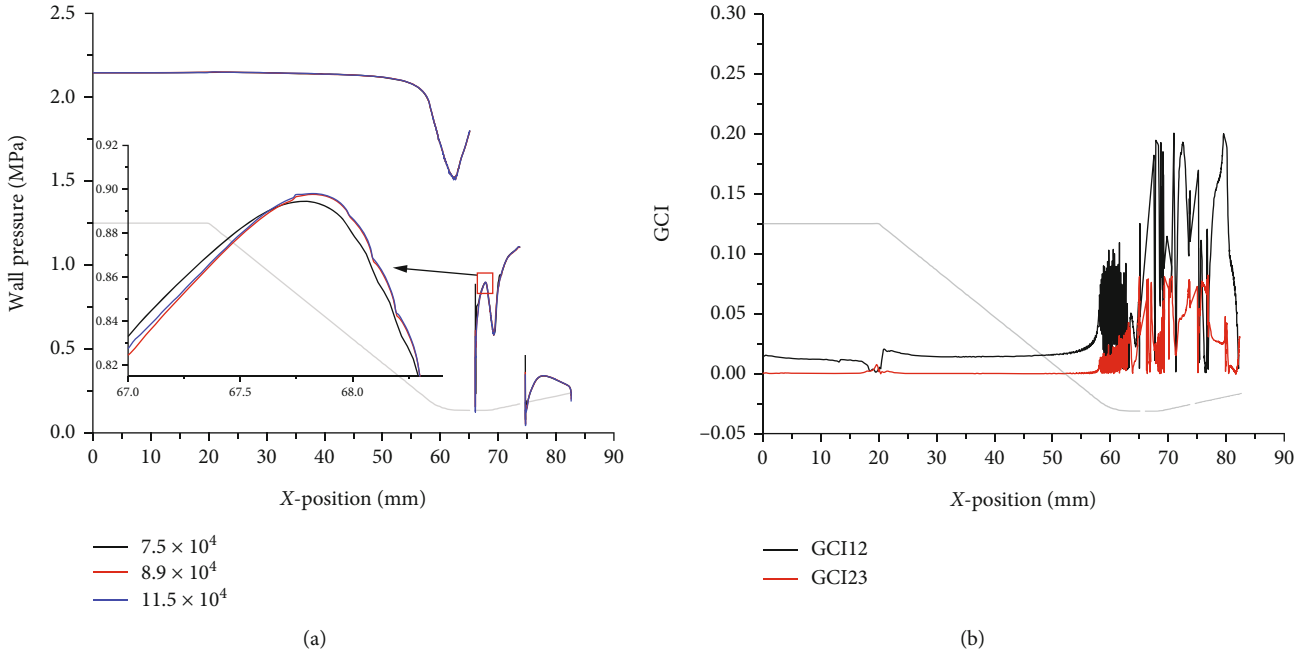
(a)

(b)

FIGURE 4: Grid independence verification: (a) wall pressure at different scales; (b) Grid Convergence Index between different scales.

extrapolated from the inside of the flow field. The ambient pressure value at the outlet is 101,325 Pa. Local mesh refinement is performed in the areas near the wall and where there are drastic changes in flow pressure.

Figure 5 compares the contour of density calculated numerically in this paper with the schlieren figure measured in Waithe and Deere's experiment. The positions of the shock wave and expansion wave in the density contour and schlieren figure are basically the same. This indicates that the numerical analysis model used in this paper is reliable for engine flow field analysis.

3.2. Three-Dimensional Calculation Verification. In the grid of the 3D model, the mean value of $y+$ is 7.8, which basically meets the calculation requirements and can better calculate the Liutex magnitude [47]. Figure 6 shows the distribution of $y+$ on the wall of the symmetry plane at $Z = 0$, in which $y+$ fluctuates greatly at the injector.

Furthermore, the 3D numerical method's precision and dependability were confirmed through Viti et al.'s schlieren experiment [48]. Viti et al.'s experiment utilized an injector with a diameter of 0.48 cm and a pressure ratio of 532 for the jet to cross flow. The primary flow had a Mach number of Ma = 4, while the Mach number of the jet was Ma = 1. The Virginia Tech supersonic wind tunnel, which operates on the blowdown principle, was used for the experiment. The tunnel has a working section measuring 23 cm × 23 cm . In the supersonic laboratory, a dual-mirror schlieren system was set up to capture spark schlieren images. An adjustable light slit, a convex lens (f—17.78 cm), and General Radio Model 1538-A Strobotac with a pulse duration of 1–2 μs make up the system. Further details regarding the experiment can be found in Ref [48]. The shock wave configuration in the vicinity of the injector was effectively recorded (see Figure 7(a)). A simulation model was developed based

on this experiment, and numerical simulations were utilizing the LES method outlined in the Numerical Methods. Upon comparing the experimental and simulation results, it was observed that the position and shape of the Mach disk, barrel shock, and separation-induced shock recorded in the results (see Figure 7(b))) closely match those of the experiment. The small vortex above the barrel shock in the simulation result is obtained by the LES method, while vortex observation using schlieren imaging which is based on the observation of density changes is limited.

4. Results and Discussion

4.1. Flow Characteristics of a Jet in Transonic Crossflow (3D LES Model Simulation). This section analyzes flow details for a case with a flow ratio of 0.067 and no chemical reaction involved. In addition to $z/d = 0$ (where d is the diameter of the injector and the origin of the coordinate system is located at the center of the injector, as shown in Figure 8), multiple x/d slices were also selected. Table 4 presents the location information of specific slices selected for the analysis of the flow details in a case with a flow ratio of 0.067, where no chemical reaction is involved. In addition to the slice at $z/d = 0$ (where d is the diameter of the injector and the origin of the coordinate system is located at the center of the injector; see Figure 8), multiple x/d slices were chosen. The momentum flux ratio J was calculated for various angles and pressure ratios to enhance the generalizability of the results.

$$J = \frac{(\rho u^2)_j}{(\rho u^2)_{pri}} = \frac{(p \Upsilon Ma^2)_j}{(p \Upsilon Ma^2)_{pri}}, \quad (10)$$

where ρ is the density, u is the velocity, Ma is the Mach

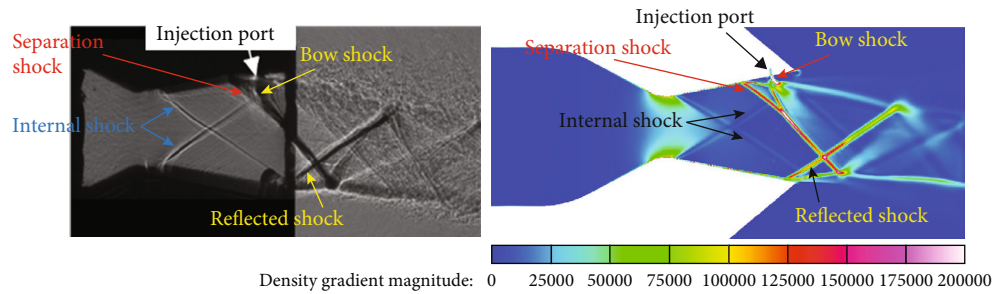Density gradient magnitude: 0 25000 50000 75000 100000 125000 150000 175000 200000

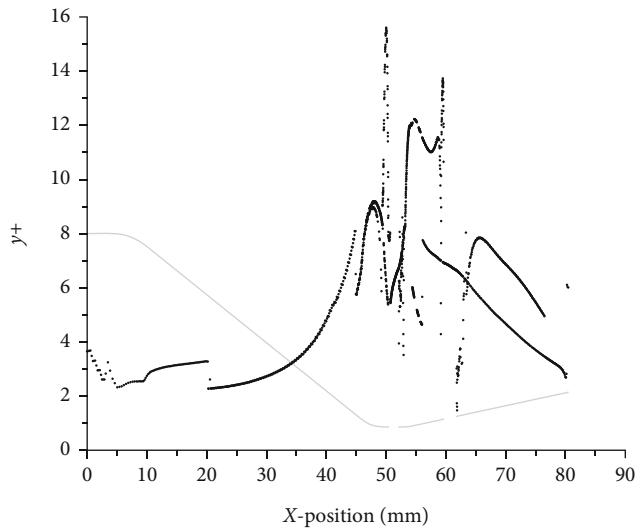Figure 5: Comparison between experimental schlieren [46] and numerical calculation.

Figure 6: $y+$ for 3D grid.

number, γ is the specific heat ratio, p is the pressure, and the subscripts j and pri denote the jet and main stream, respectively. At the throat, the momentum flux ratio between the secondary flow and the primary flow is $J = 0.34$, while at the position of the divergence section, the momentum flux ratio is $J = 0.275$. As there is a large gradient in the convergent–divergent nozzle, the crossflow momentum flux is calculated at the initial portion of the straight section using the position $x/d = -1.22$ as the calculation parameter.

Figure 9(a) depicts the Mach number contours and temperature contour on the symmetric plane. Due to the difference in crossflow and jet temperatures and the subsonic nature of the jet, no Mach disk is observed. The jet is injected at the throat, and the flow near the injector remains around $Ma = 1$, without forming any significant shock wave. The jet then flows around the injector and fills the downstream space, similar to the flow around a cylinder. Figure 9(b) shows that the fluidic throat formed by the jet can be observed in region A, and it limits the primary flow similar to the geometric throat. In the divergence section, the jet formed a significant shock wave and induced the primary flow to deflect, as observed in region B in Figure 9(b). Downstream of the injector, a high Mach number in region C is formed due to incomplete expansion of the subsonic jet, which continues to expand and perform work near the injector. This generates a shock wave, after which the velocity,

temperature, and pressure drop sharply. In the divergence section downstream of the injector, the phenomenon of primary flow bypassing the jet to fill the downstream is more noticeable, and the primary flow bypassing the injector merges downstream of the injector and continues to expand and accelerate.

In two-dimensional axisymmetric and planar studies, it is commonly believed that the jet is attached to the wall surface, resulting in a ring-shaped fluidic throat within a 360° range [9]. In three-dimensional studies, it is recognized that a distributed injector can cause the primary flow to bypass the jet, which is not attached to the wall surface. However, this does not necessarily mean that a fluidic throat cannot be formed in a three-dimensional condition. By altering the shape of the injector and increasing the number of injectors, a complete fluidic throat can still be formed.

The jet and the primary flow mix near the injector, leading to the formation of a series of vortices, as depicted in Figure 8. Figures 10 and 11 display the Liutex magnitude in various slices, with the specific positions of each slice listed in Table 3 (note: note that the results in Figures 10 and 11 are mirror images, with only half of the fluid region calculated using the XY plane as the plane of symmetry). Figure 12 illustrates the relative locations of the different slices, with S1 being the upstream slice, S7 the exit slice, and the others arranged in between. The jet is injected from the injector into the nozzle, and the upstream and edge of the jet make contact with the primary flow, leading to intense mixing. This results in the formation of strong vortices near the injector, as depicted in Figures 10(a) and 10(b). As the flow progresses, the position and shape of the vortex change, as shown in Figures 10(b) and 10(c). The main structures, including the trailing lower vortex, trailing major vortex, and horseshoe vortex, can be clearly observed. As the primary flow reaches supersonic speeds in the divergence section, the horseshoe vortex upstream of the injector in the divergence section becomes more pronounced and develops towards the nozzle outlet, as shown in Figures 10(d)–10(f). In Figure 10, the intensity of the vortex decreases significantly in comparison to (b) and (e), which is caused by different momentum-flux ratios. At A, B, and C, the Liutex magnitude is 587139, 1720026, and 599301, respectively, in Figure 10(b)). However, in Figure 10(e)), the Liutex magnitude at A, B, C, and D is 605786, 9160644, 420587, and 375908, respectively.

Figure 11 shows that on the Y-Z plane, the vortices are predominantly distributed near the injector. Upstream of

(a)

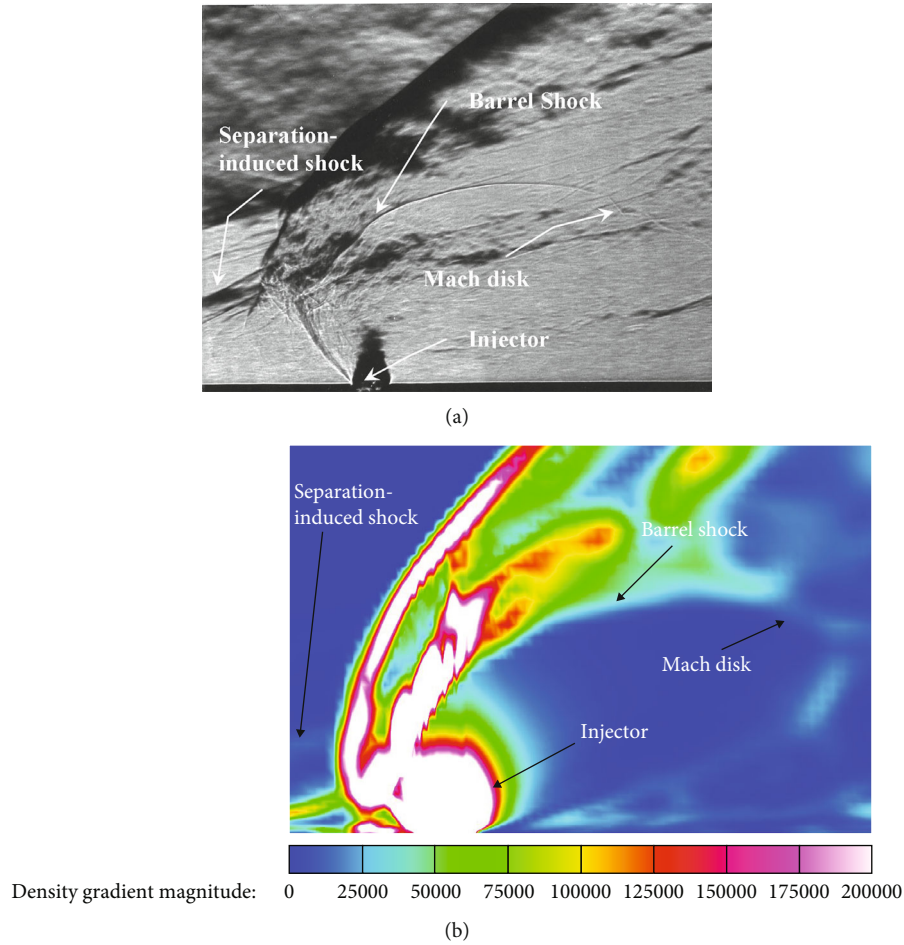Density gradient magnitude: 0   25000 50000 75000 100000 125000 150000 175000 200000

(b)

FIGURE 7: Experimental schlieren photograph and CFD solutions on the symmetry plane: (a) experimental schlieren photograph [42]; (b) CFD density gradient calculated via LES.
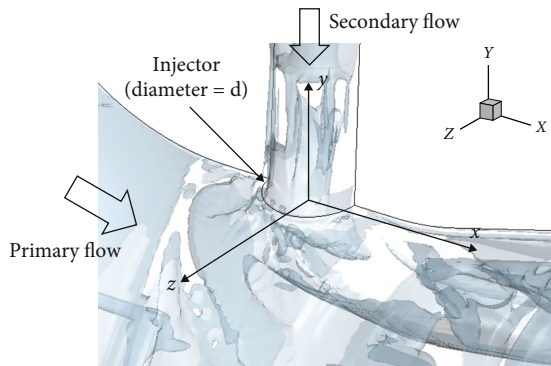

FIGURE 8: Vortex structure near the injector, Liutex magnitude = 5000.

TABLE 4: Slice location information.

Slice	x/d
S1	0
S2	0.85
S3	2.10
S4	3.52
S5	5.34
S6	6.53
S7	8.64

the injector is the horseshoe vortex, with surface trailing vortices on both sides, and the downstream exhibits the trailing lower vortex with high vortex intensity. The intensity of the vortex near the injector in the divergence section is significantly weaker than that at the throat.

Combining the analysis of Figures 12 and 13, it can be observed the jet causes extrusion and interference of the crossflow, resulting in the formation of a horseshoe vortex upstream of the jet The horseshoe vortex progresses later-

ally along the wall, moving away from the $Z = 0$ plane (symmetry plane). As the flow progresses through the divergence section, the horseshoe vortex becomes increasingly pronounced and extends all the way to the nozzle outlet. The presence of the surface trailing vortex is attributed to the crossflow around the jet near the injector, and it is visible at the interface between the filling primary flow and the jet. When the momentum flux ratio is low, the jet injection depth is also low, and the trailing lower vortex and trailing major vortex are in close proximity to each other. Upon observation, it becomes apparent that the trailing lower vortex has a greater intensity than the
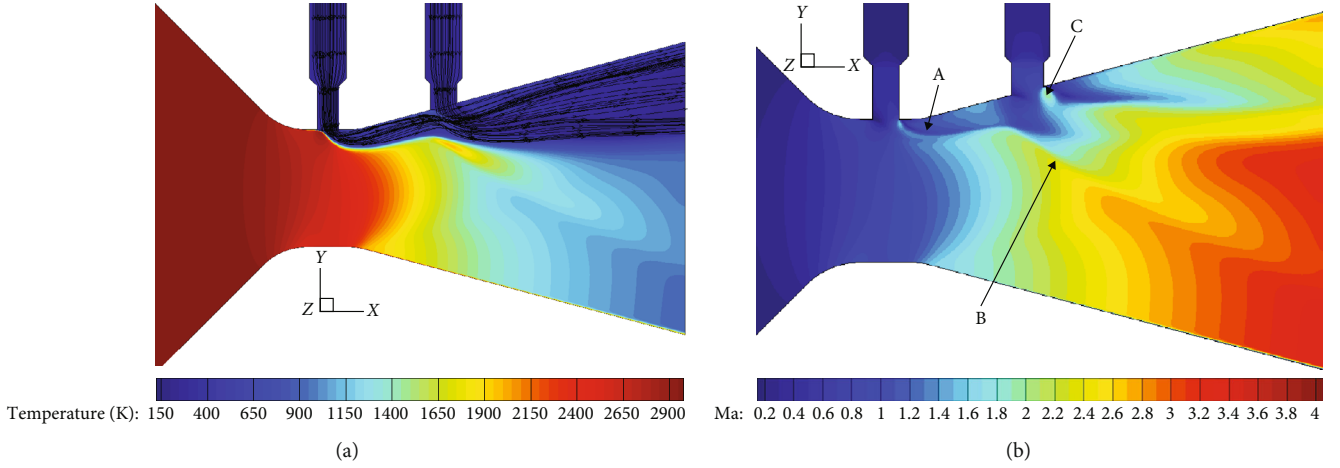
Temperature (K): 150 400 650 900 1150 1400 1650 1900 2150 2400 2650 2900

(a)

Ma: 0.2 0.4 0.6 0.8 1 1.2 1.4 1.6 1.8 2 2.2 2.4 2.6 2.8 3 3.2 3.4 3.6 3.8 4

(b)

Figure 9: Contours of symmetric plane: (a) temperature contour and streamlines, $z/d = 0$; (b) Mach number contour, $z/d = 0$.

trailing major vortex. Furthermore, the trailing lower vortex extends further in the X direction when compared to the trailing major vortex. This observation suggests that when the momentum flux ratio is small, the trailing lower vortex becomes dominant vortex in terms of intensity, overshadowing the trailing major vortex. As the vortices progress, the surface trailing vortices merge into trailing major vortex, which is accompanied by the merge of multiple trailing vortices.

4.2. Improvement of Nozzle Performance by Oxidative Jet Injection (2D RANS Model Simulation). In this study, the axial dynamic thrust F_{Dx} and radial thrust F_{Dy} can be determined by integrating the flow rate and velocity at the nozzle outlet interface, which can then be used to calculate the thrust vector angle. The axial velocity component is denoted by v_x, and the radial velocity component is denoted by v_y. FD represents the dynamic thrust of the nozzle, $\dot{m}$ represents the mass flow rate of the nozzle, and θ represents the thrust vector angle.

$$
\begin{aligned}
F_D &= \dot{m}v = \sum_{i=1}^{n} \dot{m}_i \bar{v}_i, \\
F_{Dx} &= \dot{m}v_x = \sum_{i=1}^{n} \dot{m}_i \bar{v}_{ix}, \\
F_{Dy} &= \dot{m}v_y = \sum_{i=1}^{n} \dot{m}_i \bar{v}_{iy}, \\
\theta &= \arctan \frac{F_{Dy}}{F_{Dx}}.
\end{aligned}
\tag{11}
$$

When calculating the combustion efficiency, we can obtain the combustion efficiency η by comparing the component mass at the nozzle outlet with the original component mass of the primary flow. $\dot{m}_{if}$ and $\dot{m}_{ib}$ represent the mass of the components before and after the reaction, respectively.

$$
\eta = \frac{\dot{m}_{if} - \dot{m}_{ib}}{\dot{m}_{if}}.
\tag{12}
$$

This section presents a quantitative analysis of the thrust vector angle, outlet pressure, secondary combustion efficiency, and nozzle combustion pressure. In the plotted curve, f_m represents the flow ratio of the secondary flow to the primary flow, and the flow ratio discussed in the article is the ratio of flow between a single injection port and the primary flow. The letter D represents injection in the divergence section, while $D + T$ represents injection in both the throat and divergence section simultaneously.

In terms of thrust vector angle adjustment, Figure 14(a) demonstrates that injecting the secondary flow in the divergence section changes the vector angle. As the flow ratio (i.e., the secondary flow rate) increases, the vector angle first increases and then decreases, forming a peak. The magnitude of the peak vector angle and the corresponding flow ratio is influenced by the combination of the secondary flow working medium and the injection port position. For the four cases studied in this paper, the peak vector angles increase in the following order as the flow ratio increases: Case 2 (pure oxygen injection in the divergence section), Case 1 (nitrogen injection in the divergence section), Case 3 (nitrogen injection in the divergence section and throat), and Case 4 (pure oxygen injection in the divergence section and throat), with corresponding vector angles of 5.51°, 5.07°, 4.53°, and 4.18°, respectively. The peak values correspond to the flow ratios of 0.15, 0.175, 0.175, and 0.15. This indicates that the flow ratio corresponding to the peak point of the vector angle of oxygen in the divergence section is advanced by 14.3% (O_2—0.15, N_2—0.175). The results indicate that injecting pure oxygen in the divergence section only has the best vector adjustment effect, with the highest peak vector angle and vector angle at each flow rate and requiring a smaller secondary flow rate to achieve the peak vector angle than nitrogen. However, injecting pure oxygen in both the divergence section and throat simultaneously (Case 4)
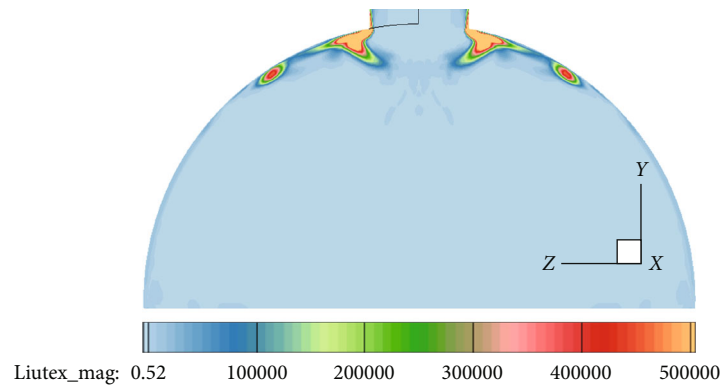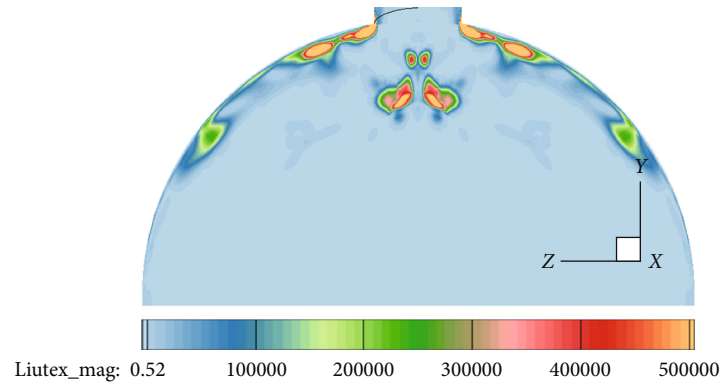
(a)
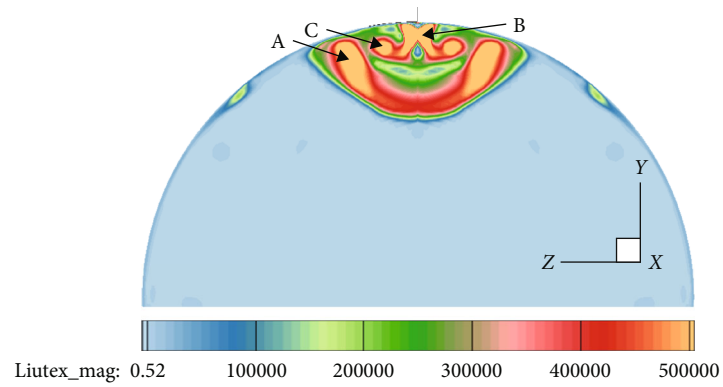
(b)
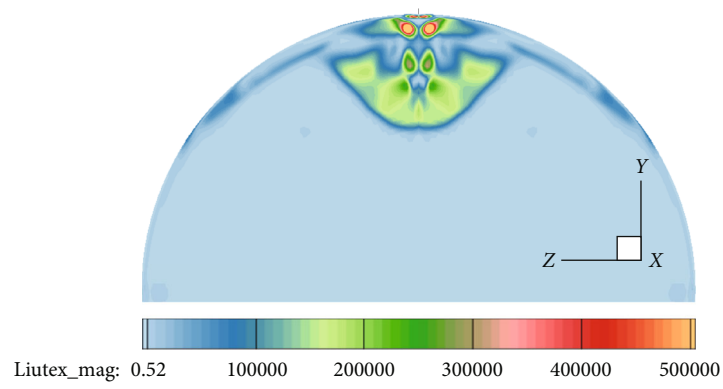
(c)

(d)
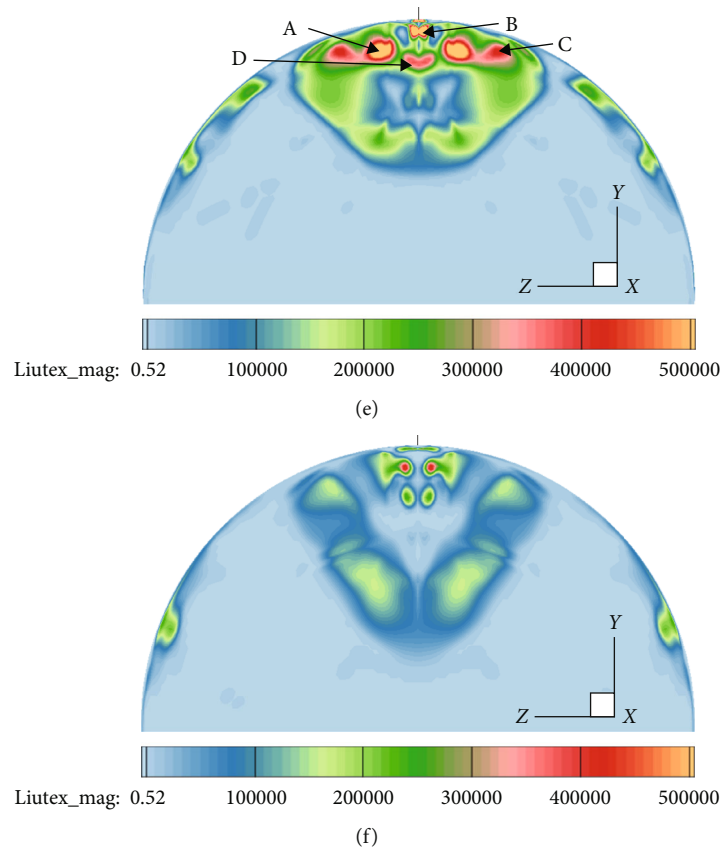
FIGURE 10: Continued.

(e)

(f)

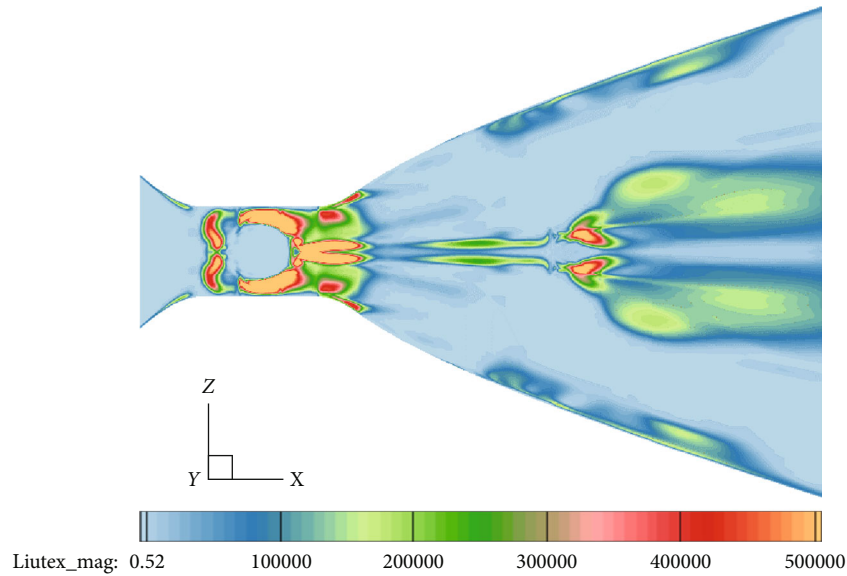FIGURE 10: Liutex magnitude contours on different slices: (a) S1; (b) S2; (c) S3; (d) S5; (e) S6; (f) S7.

FIGURE 11: Liutex magnitude contours on $y/d = 0.11$.

results in the worst vector adjustment effect, with a decrease in the peak vector angle compared to nitrogen and a smaller vector angle at low flow ratios.

Regarding the regulation of the nozzle's expansion state, Figure 14(b) shows that injecting secondary flow at the throat or divergence section increases the nozzle's outlet pressure by increasing its total flow rate. Furthermore, pure oxygen injection increases the outlet pressure of the nozzle more than nitrogen injection does. The analysis indicates that, after pure oxygen injection, the primary flow undergoes
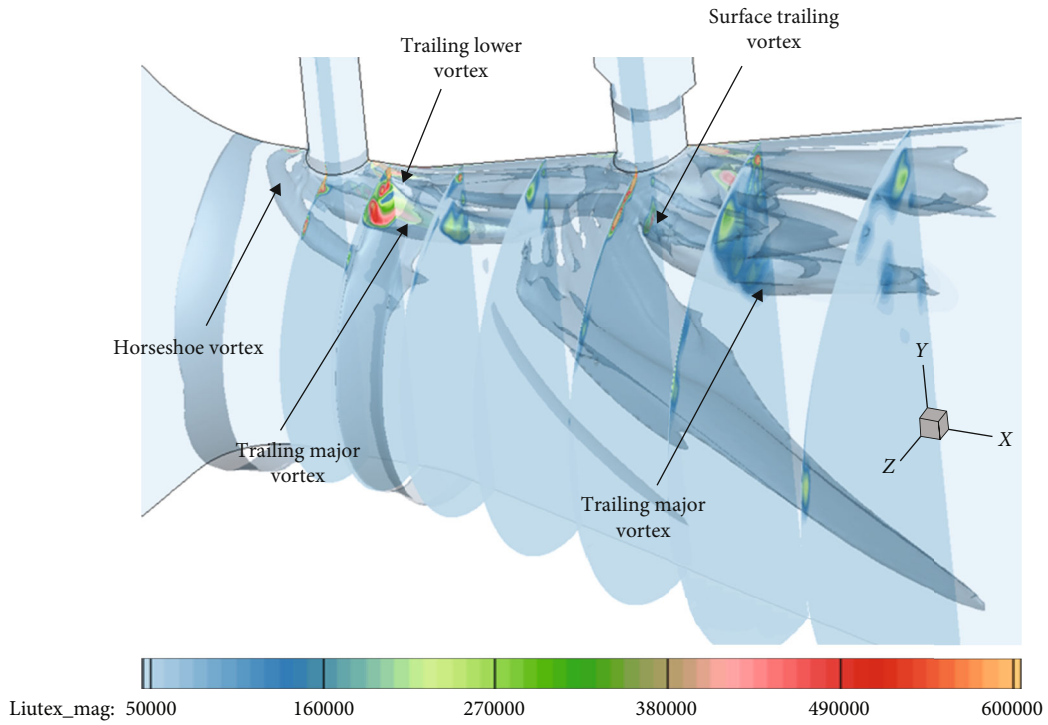
FIGURE 12: Vortex structure and vortex evolution, Liutex magnitude = 100,000.
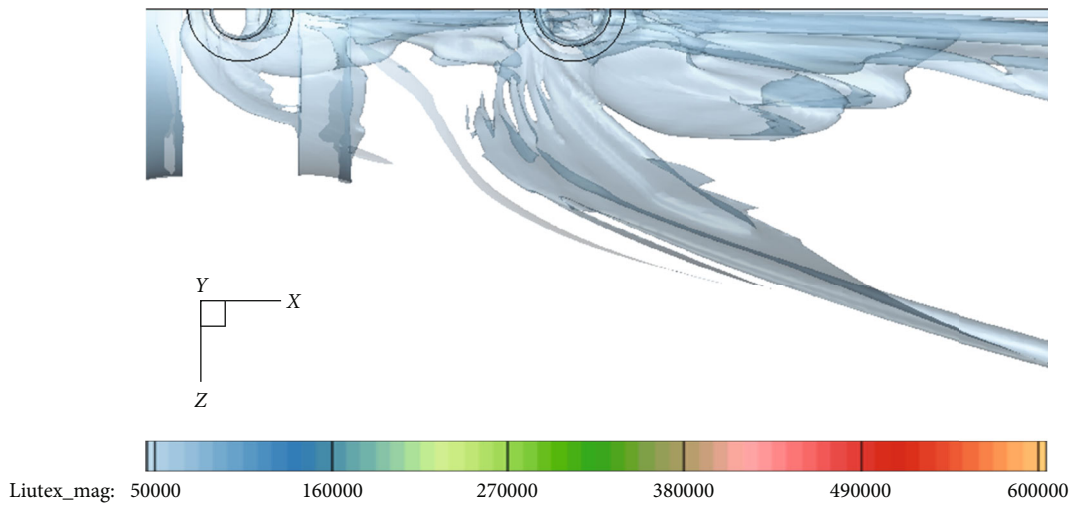

FIGURE 13: Liutex isosurface with magnitude = 100,000.

secondary combustion near the injection ports, converting part of its chemical energy into heat energy, which expands and does work, thereby increasing the outlet pressure. Among the four cases presented in this paper, Case 4 (pure oxygen injection in the divergence section and throat) has the most significant effect on the outlet pressure. This improvement is due to the increased total flow of the jet and the conversion of more chemical energy into heat energy, which expands and does work.

With an increase in the flow ratio, the efficiency of secondary combustion of combustible components (H_2 and CO) in the flow gradually increases, as depicted in Figure 14(c). However, secondary combustion is generally not very efficient. In Case 2 (nitrogen injection in the divergence section and throat), when the flow ratio is 0.15, the combustion efficiency of H_2 and CO in the flow is only 3.4% and 5.8%, respectively. Increasing the flow ratio of pure oxygen results in an increase in oxygen concentration, which leads to an increase in secondary combustion efficiency of reducing components in the primary flow. This increase in efficiency is due to the increase in the chemical reaction rate caused by the increase in oxidative concentration. Therefore,
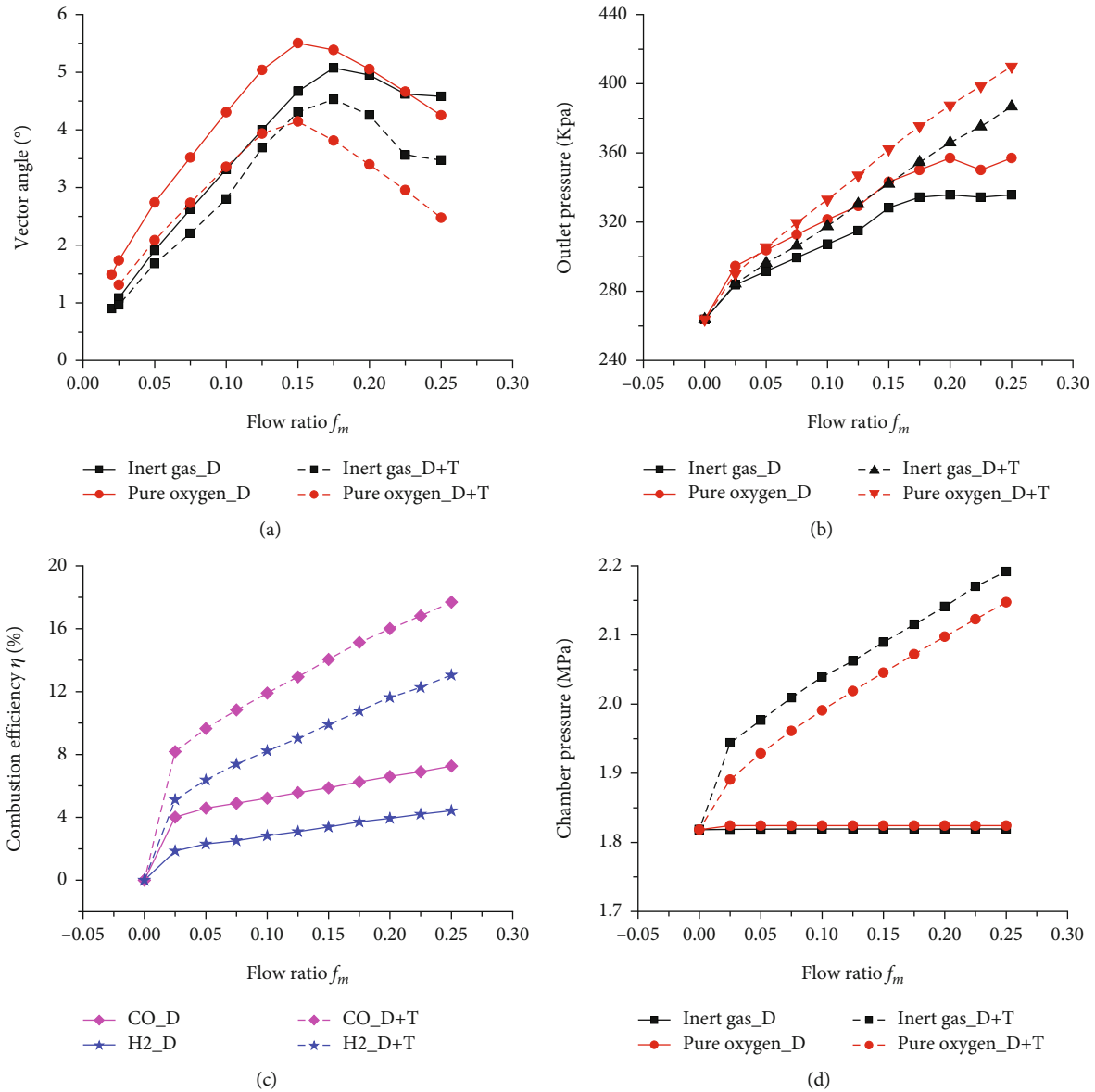
FIGURE 14: Results of nozzle performance: (a) vector angle; (b) outlet pressure; (c) secondary combustion efficiency; (d) combustion chamber pressure.

by injecting pure oxygen in the divergence section, the secondary combustion efficiency increases by more than twice. In addition to increasing oxidative concentration, the jet injected at the throat reacts further with the gas during the flow process.

The principle of the aerodynamic throat or fluidic throat involves injecting secondary flow at the throat, which compresses the primary flow, reducing the effective throat area of the primary flow and increasing the pressure of the combustion chamber. Figure 14(d) shows that injecting pure oxygen at the throat results in a lower pressure increase in the combustion chamber compared to injecting nitrogen. This is due to the fact that pure oxygen reacts with the primary flow at the throat, leading to a reduced penetration effect. Injecting secondary flow in the divergence section, on the other hand, has no effect on the pressure of the combustion chamber.

4.3. Analysis of the Vector Control Effect Using Two-Dimensional Calculations.
In this section, we will discuss and analyze in detail the temperature, pressure, and Mach number distributions of typical cases.

4.3.1. Injecting Pure Oxygen in the Divergence Section.
The secondary flow was injected into the divergence section for both the pure oxygen case and nitrogen case with a flow ratio of 0.125, and a comparative analysis was conducted, as shown in Figures 15 and 16. Upon injecting pure oxygen, it reacts with the primary flow in the contact region, and a narrow reaction zone extends along the flow direction to the nozzle outlet, as depicted in Figure 15(a). The maximum temperature in the reaction region reaches 4000 K, which is higher than the primary flow's 3000 K. However, due to the high flow speed in the divergence section, most oxygen remains unreacted, resulting in little temperature variation
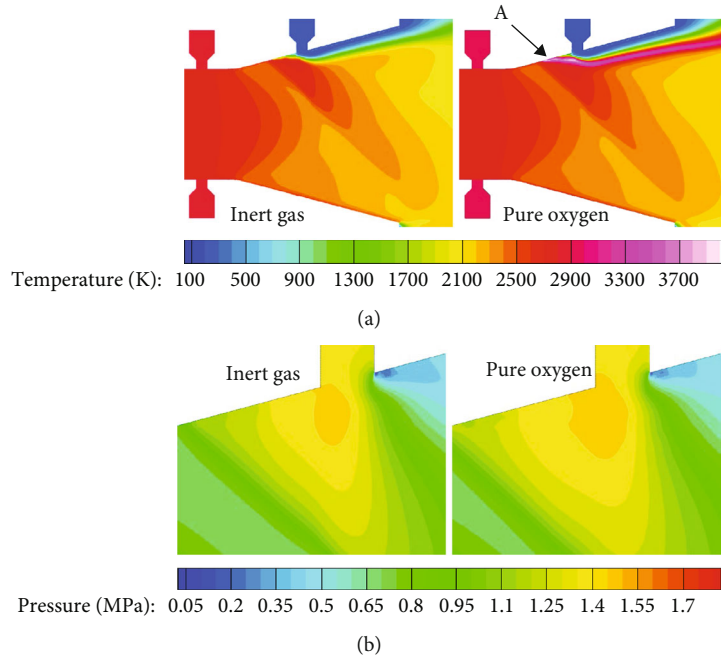
Temperature (K): 100 500 900 1300 1700 2100 2500 2900 3300 3700

(a)

Pressure (MPa): 0.05 0.2 0.35 0.5 0.65 0.8 0.95 1.1 1.25 1.4 1.55 1.7

(b)

FIGURE 15: Contour of flow field injected in divergence section. (a) temperature Contours. (b) Contours of pressure for local region.

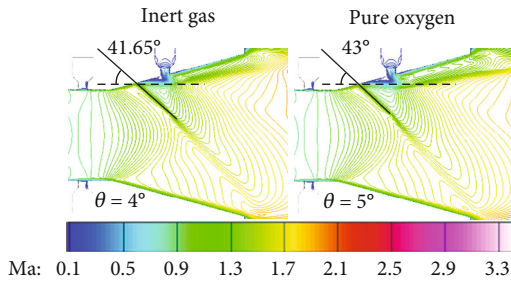Ma: 0.1 0.5 0.9 1.3 1.7 2.1 2.5 2.9 3.3

FIGURE 16: Mach Contour of flow field injected in divergence section.

FIGURE 17: Pressure of upper wall (injected in divergence).

in other regions. Apart from point A in Figure 15(a), the secondary flow with normal temperature separates most of the high-temperature reaction zone from the wall surface.

When pure oxygen is injected, the high-pressure region near the upstream part of the injection port tends to expand, as illustrated in Figure 15(b). This is because secondary combustion generates a local high-temperature and high-pressure region, which directly leads to the upstream movement of the initial shock position, as shown in Figures 15(b) and 17. Furthermore, the initial angle of the oblique shock wave increases from 41.65° for nitrogen injection to 43° for pure oxygen injection, as displayed in Figure 16. The changes in initial position and initial angle result in the pure oxygen case having a larger vector angle than the nitrogen case. As the flow ratio increases, the oblique shock wave begins to reflect on the opposite side wall, causing the peak of the vector angle to appear when the oblique shock wave reflects at the nozzle outlet on the opposite wall.
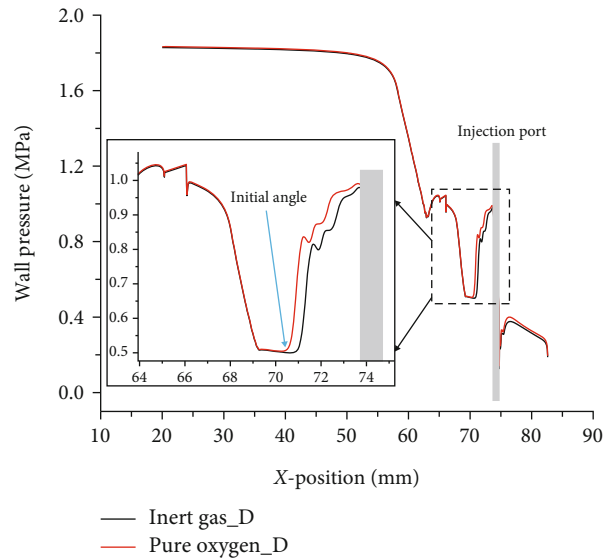
4.3.2. Injecting Pure Oxygen in the Divergence Section and Throat. In the divergence section and throat, both the secondary flow and pure oxygen were injected simultaneously. Comparative analysis was carried out for pure oxygen and nitrogen cases with a flow ratio of 0.125 (i.e., the injection port's flow rate was 0.125 times that of the primary flow). The results, presented in Figure 18(a)), showed that injecting pure oxygen resulted in a significant high-temperature region, up to 4400 K, in the contact region with the primary flow. However, since most of the oxygen did not react with the primary flow, little difference in temperature was observed in other regions. The high-pressure and high-
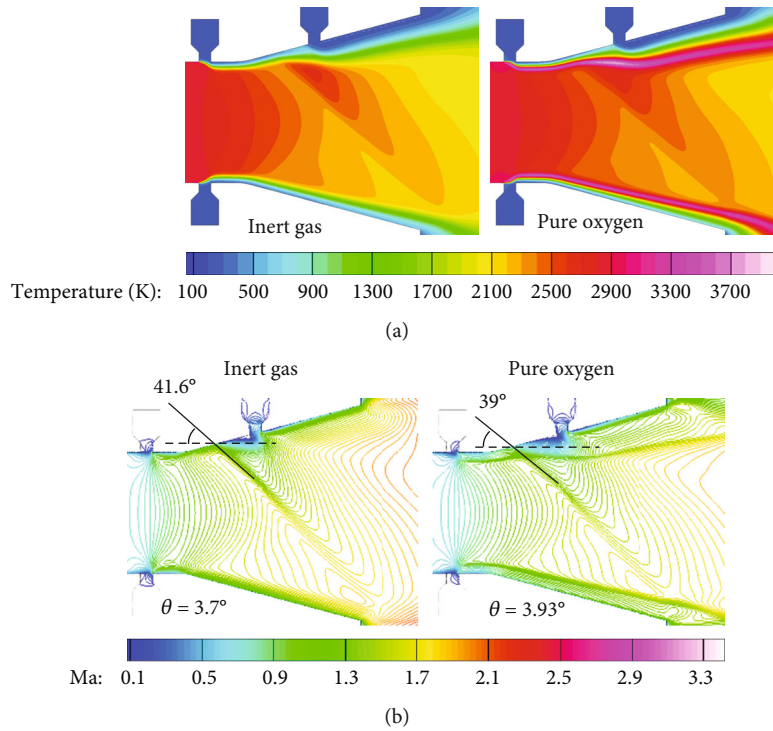
(a)

(b)

FIGURE 18: Contour of flow field injected in the divergence section and the throat: (a) temperature contours; (b) Mach contours.
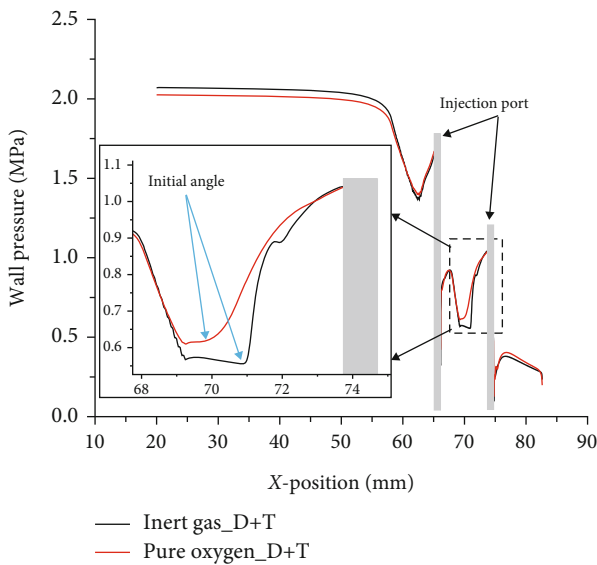

FIGURE 19: Pressure of upper wall (injected in the divergence section and throat).

temperature region near the injection port in the divergence section caused the initial position of the shock wave to move upstream, which was more pronounced than injecting oxygen only in the divergence section (Figures 17 and 19). As the oxygen reacted with the primary flow's components, the secondary flow's components were consumed, and the squeezing effect of the jet on the primary flow at the throat weakened, leading to a reduction in the regulation effect on the combustion chamber pressure. The initial angle of the

oblique shock wave for pure oxygen injection was smaller, only 39°, and the vector angle was 0.23° higher than that of nitrogen injection (Figure 18(b)). The primary reason for the higher vector angle in the case of pure oxygen injection was the upstream movement of the shock wave's initial position.

5. Conclusions

This paper investigates the flow details and vortex structure of jets in the divergence section and throat using 3D large eddy simulation. Additionally, a 2D model is developed to analyze the vector regulation effect of the reaction between the pure oxygen jet and the primary air flow, incorporating a simple chemical reaction. Based on the findings, the following conclusions can be drawn:

(1) In the study of vector regulation with small momentum flux ratio, the horseshoe vortex is obvious. Trailing lower vortex replaces trailing major vortex to become the highest magnitude vortex in the system. The trailing top vortex is not observed

(2) Based on the research conducted in this paper, it was found that injecting pure oxygen in the divergence section leads to the formation of a high-temperature and high-pressure region near the injection port, resulting in an upstream movement of the initial position of the shock wave and an increase in the initial angle of the shock wave. Additionally, the vector angle decreases and then increases as the flow rate ratio increases, with the

turning point being the reflection of shock waves on the opposite wall. The maximum vector angles for the four different cases are ranked in descending order as follows: Case 2 (pure oxygen injection in the divergence section) > Case 1 (nitrogen injection in the divergence section) > Case 3 (nitrogen injection in the divergence section and throat) > Case 4 (pure oxygen injection in the divergence section and throat), with corresponding vector angles of 5.51°, 5.07°, 4.53°, and 4.18°, respectively. When the secondary flow is introduced only in the divergence section, the flow ratio corresponding to the peak point in the pure oxygen case is approximately 14.3% (O_2—0.15, N_2—0.175) earlier than that in the nitrogen case

(3) The presence of pure oxygen at the throat results in a thinner shear layer of the secondary flow, which negatively affects the pressure regulation of the combustion chamber and leads to a loss of approximately 2%

(4) The efficiency of secondary combustion of combustible components in the flow gradually increases with an increase in the flow ratio. However, it is noteworthy that secondary combustion is generally not very efficient, usually not exceeding 10%

Data Availability

Data are available on request.

Conflicts of Interest

The authors declare that there is no conflict of interest regarding the publication of this paper.

Acknowledgments

References

[1] C. Guo, Z. Wei, K. Xie, D. Yan, and N. Wang, "One-dimensional theoretical analysis of dilute particle–gas swirling flow in the Laval nozzle," *AIAA Journal*, vol. 56, no. 3, pp. 1277–1283, 2018.

[2] J. Sapkota, X. Yi, and H. Sun, "Numerical study on response characteristics of solid rocket pintle motor," *Journal of Aerospace Technology and Management*, vol. 11, 2019.

[3] P. Paul, P. P. John, A. S. Nair, M. Joe Paul Martin, and H. D. Kim, "Numerical simulation on optimization of pintle base shape in planar expansion-deflection nozzles," *Journal of Spacecraft and Rockets*, vol. 57, no. 3, pp. 539–548, 2020.

[4] D. Yan, Z. Wei, K. Xie, and N. Wang, "Simulation of thrust control by fluidic injection and pintle in a solid rocket motor," *Aerospace Science and Technology*, vol. 99, article 105711, 2020.

[5] A. Song, N. Wang, J. Li, B. Ma, and A. X. Chen, "Transient flow characteristics and performance of a solid rocket motor with a pintle valve," *Chinese Journal of Aeronautics*, vol. 33, no. 12, pp. 3189–3205, 2020.

[6] V. Saravanan, J. Ko, S. Lee, N. Murugan, and V. R. Sanal Kumar, "Conceptual aerodynamic design of pintle nozzle for variable-thrust propulsion," *International Journal of Aeronautical and Space Sciences*, vol. 21, no. 1, pp. 1–14, 2020.

[7] M. Ji and H. Chang, "Modeling and dynamic characteristics analysis on solid attitude control motor using pintle thrusters," *Aerospace Science and Technology*, vol. 106, article 106130, 2020.

[8] D.-S. Ha and H. J. Kim, "Dynamic characteristic modeling and simulation of an aerospike-shaped pintle nozzle for variable thrust of a solid rocket motor," *Acta Astronautica*, vol. 201, pp. 364–375, 2022.

[9] K. Xie, X. Chen, J. Li, and Y. Liu, *Fluidic Nozzle Throats in Solid Rocket Motors*, Springer Nature Singapore Pte Ltd. and National Defense Industry Press, 2019.

[10] D. Yan, Z. Wei, K. Xie, C. Guo, W. Tang, and N. Wang, "Study of the vortex structure of a subsonic jet in an axisymmetric transonic nozzle," *Physics of Fluids*, vol. 32, no. 7, article 076109, 2020.

[11] A. Ali, C. Rodriguez, A. Neely, and J. Young, "Combination of fluidic thrust modulation and vectoring in a 2d nozzle," in *48th AIAA/ASME/SAE/ASEE Joint Propulsion Conference & Exhibit*, Atlanta, Georgia, 2012.

[12] C. Guo, Z. Wei, K. Xie, and N. Wang, "Thrust control by fluidic injection in solid rocket motors," *Journal of Propulsion and Power*, vol. 33, no. 4, pp. 815–829, 2017.

[13] M. Ferlauto and R. Marsilio, "Computational investigation of injection effects on shock vector control performance," in *2018 Joint Propulsion Conference*, Cincinnati, Ohio, 2018.

[14] E. Lee, H. Kang, and S. Kwon, "Demonstration of thrust vector control by hydrogen peroxide injection in hybrid rockets," *Journal of Propulsion and Power*, vol. 35, no. 1, pp. 109–114, 2019.

[15] Y. Maruyama, M. Sakata, and Y. Takahashi, "Performance analyses of fluidic thrust vector control system using dual throat nozzle," *AIAA Journal*, vol. 60, no. 3, pp. 1730–1744, 2022.

[16] B. Semlitsch and M. Mihăescu, "Fluidic injection scenarios for shock pattern manipulation in exhausts," *AIAA Journal*, vol. 56, no. 12, pp. 4640–4644, 2018.

[17] K. Younes and J.-P. Hickey, "Fluidic thrust shock-vectoring control: a sensitivity analysis," *AIAA Journal*, vol. 58, no. 4, pp. 1887–1890, 2020.

[18] P. Sethuraman, V. Ram, T. H. Kim, and H. D. Kim, "Control of the oscillations of shock train using boundary layer suction," *Aerospace Science and Technology*, vol. 118, article 107012, 2021.

[19] B. Semlitsch and M. Mihăescu, "Evaluation of injection strategies in supersonic nozzle flow," *Aerospace*, vol. 8, no. 12, p. 369, 2021.

[20] A. Neely, F. Gesto, and J. Young, "Performance studies of shock vector control fluidic thrust vectoring," in *43rd AIAA/ASME/SAE/ASEE Joint Propulsion Conference & Exhibit*, Cincinnati, OH, 2007.

[21] C. Wang, C. Cheng, K. Cheng, and L. Xue, "Unsteady behavior of oblique shock train and boundary layer interactions," *Aerospace Science and Technology*, vol. 79, pp. 212–222, 2018.

[22] Q. Zhang, K. Wang, J. Wang, X. Qiao, and W. Fan, "Experimental research on vector control features of a pulse detonation tube with fluidic nozzle," *Aerospace Science and Technology*, vol. 116, article 106456, 2021.

[23] F. Forghany, M. Taeibe-Rahni, and A. Asadollahi-Ghohieh, "Numerical investigation of freestream flow effects on thrust vector control performance," *Ain Shams Engineering Journal*, vol. 9, no. 4, pp. 3293–3303, 2018.

[24] C. He, J. Li, Y. Li, and J. Liang, "Influence of secondary injection parameters on performance of shock vector control nozzle," in *21st AIAA International Space Planes and Hypersonics Technologies Conference*, Xiamen, China, 2017.

[25] K. Younes, A. Grenke, J.-P. Hickey, M. Gagnon, and B. Elzein, "Enhanced delayed detached eddy simulations of shock-vector control," in *23rd AIAA International Space Planes and Hypersonic Systems and Technologies Conference*, Montreal, Quebec, Canada, 2020.

[26] Y. Cheng, N. Wang, K. Xie, and C. Guo, "Effect of secondary injection reaction thermal resistance on thrust vector control in divergent section," in *2018 Joint Propulsion Conference*, Cincinnati, Ohio, 2018.

[27] H. Ko and W.-S. Yoon, "Performance analysis of secondary gas injection into a conical rocket nozzle," *Journal of Propulsion and Power*, vol. 18, no. 3, pp. 585–591, 2002.

[28] Y.-Q. Wang, F. Xiao, S. Lin, and Y.-Z. Zhou, "Numerical investigation of droplet properties of a liquid jet in supersonic crossflow," *International Journal of Aerospace Engineering*, vol. 2021, Article ID 8828015, 17 pages, 2021.

[29] Y.-z. Zhou, F. Xiao, Q.-l. Li, and C.-y. Li, "Simulation of elliptical liquid jet primary breakup in supersonic crossflow," *International Journal of Aerospace Engineering*, vol. 2020, Article ID 6783038, 12 pages, 2020.

[30] Ansys Inc, *User's Guide*, Ansys Inc, Canonsburg, 2017, https://en.wikipedia.org/wiki/Ansys.

[31] B. F. Magnussen and B. H. Hjertager, "On mathematical modeling of turbulent combustion with special emphasis on soot formation and combustion," *Symposium (International) on Combustion*, vol. 16, no. 1, pp. 719–729, 1977.

[32] D. Li and W. Kexin, "Numerical study on rod thrust vector control for physical applications," *International Journal of Aerospace Engineering*, vol. 2021, Article ID 6963728, 15 pages, 2021.

[33] L. Y. Hou, B. Weigand, and M. Banica, "Effects of staged injection on supersonic mixing and combustion," *Chinese Journal of Aeronautics*, vol. 24, no. 5, pp. 584–589, 2011.

[34] H. Versteeg and W. Malalasekera, "An introduction to computational fluid dynamics: the finite volume method," in *Turbulence and Its Modelling*, pp. 40–115, Pearson Prentice Hall, Edinburgh Gate, 2007.

[35] F. R. Menter, "Two-equation eddy-viscosity turbulence models for engineering applications," *AIAA Journal*, vol. 32, no. 8, pp. 1598–1605, 1994.

[36] Ansys Inc, *Theory Guide*, Ansys Inc, Canonsburg, 2017, https://en.wikipedia.org/wiki/Ansys.

[37] F. Nicoud and F. Ducros, "Subgrid-scale stress modelling based on the square of the velocity gradient tensor," *Flow, Turbulence and Combustion*, vol. 62, no. 3, pp. 183–200, 1999.

[38] S. V. Patankar, *Numerical Heat Transfer and Fluid Flow*, Hemisphere Publishing, Washington, D.C, 1980.

[39] C. Q. Liu, Y. Q. Wang, Y. Yang, and Z. W. Duan, "New omega vortex identification method," *Science China Physics, Mechanics & Astronomy*, vol. 59, no. 8, article 684711, 2016.

[40] X. Dong, Y. Wang, X. Chen, Y. Dong, Y. Zhang, and C. Liu, "Determination of epsilon for omega vortex identification method," *Journal of Hydrodynamics*, vol. 30, no. 4, pp. 541–548, 2018.

[41] Y. Gao and C. Liu, "Rortex and comparison with eigenvalue-based vortex identification criteria," *Physics of Fluids*, vol. 30, no. 8, article 085107, 2018.

[42] X. Dong, Y. Gao, and C. Liu, "New normalized Rortex/vortex identification method," *Physics of Fluids*, vol. 31, no. 1, article 011701, 2019.

[43] C. Liu, Y.-s. Gao, X.-r. Dong et al., "Third generation of vortex identification methods: omega and Liutex/Rortex based systems," *Journal of Hydrodynamics*, vol. 31, no. 2, pp. 205–223, 2019.

[44] D. C. Wilcox, "Comparison of two-equation turbulence models for boundary layers with pressure gradient," *AIAA Journal*, vol. 31, no. 8, pp. 1414–1421, 1993.

[45] P. J. Roache, "Perspective: a method for uniform reporting of grid refinement studies," *Journal of Fluids Engineering*, vol. 116, no. 3, pp. 405–413, 1994.

[46] K. Waithe and K. Deere, "An Experimental and computational investigation of multiple injection ports in a convergent-divergent nozzle for fluidic thrust vectoring," in *21st AIAA Applied Aerodynamics Conference*, Orlando, Florida, 2003.

[47] J.-m. Zhan, Y.-t. Li, W.-h. O. Wai, and H. Wen-qing, "Comparison between the Q criterion and Rortex in the application of an in-stream structure," *Physics of Fluids*, vol. 31, no. 12, article 121701, 2019.

[48] V. Viti, R. Neel, and J. A. Schetz, "Detailed flow physics of the supersonic jet interaction flow field," *Physics of Fluids*, vol. 21, no. 4, article 046101, 2009.